Aalborg Universitet

AALBORG UNIVERSITY

DENMARK

On the Fully-Developed Heat Transfer Enhancing Flow Field in Sinusoidally, Spirally Corrugated Tubes Using Computational Fluid Dynamics

Hærvig, Jakob; Sørensen, Kim; Condra, Thomas Joseph

On the Fully-Developed Heat Transfer Enhancing Flow Field in Sinusoidally, Spirally Corrugated Tubes Using Computational Fluid Dynamics

J. Hærvig[a,*], K. Sørensen[a], T.J. Condra[a]

[a]*Aalborg University, Department of Energy Technology, Pontoppidanstræde 111, DK-9220 Aalborg, Denmark*

Abstract

A numerical study has been carried out to investigate heat transfer enhancing flow field in 28 geometrically different sinusoidally, spirally corrugated tubes. To vary the corrugation, the height of corrugation e/D and the length between two successive corrugated sections p/D are varied in the ranges 0 to 0.16 and 0 to 2.0 respectively. The 3D Unsteady Reynolds-averaged Navier-Stokes (URANS) equations combined with the transition SST turbulence model are solved using the finite volume method to obtain the fully-developed flow field in a repeatable section of the heat exchangers at a constant wall temperature and at Re = 10,000. By studying the wide range of geometrically different tubes, the flow conditions vary significantly.

At low corrugation heights, only a weak secondary flow centred in the corrugated section is present. At higher corrugations heights, the tangential velocity component increases and eventually exceeds the axial velocity component causing the highest pressure to be located at the centre of the corrugated section. At these high corrugation heights, a further increase in corrugation height will at best only result in a small increase in Nusselt number but at a significantly higher pressure loss. To assess the performance as a heat exchanger, the ratio of enhanced Nusselt number to enhanced friction factor $\eta = (\mathrm{Nu}/\mathrm{Nu_s})/(f/f_s)^{1/3}$ compared to the non-corrugated tube is used. Using this parameter, the simulations show a decrease in performance at higher corrugation heights. To link the detailed flow fields to the performance as a heat exchanger, non-dimensional correlations for heat transfer, pressure loss, and performance parameter are given.

Keywords: Fully-developed flow, Heat transfer, Pressure loss, 3D CFD, Swirling flow, Re-circulation zones, Parameter variation

1. Introduction

Transferring heat through a straight tube is used in numerous applications. These applications include, but are not limited to, power generation, air-conditioning, petrochemical, and diary applications. Two distinct different techniques for enhancing heat transfer are commonly used; namely a passive or active, where the active requires additional power input whereas the passive does not. Therefore, the passive technique is commonly used where the geometry is altered in a more of less sophisticated manner deforming the thermal boundary layer, creating recirculating local flow structures, or larger secondary flow structures flowing tangentially to the main flow. All these phenomena affect both heat transfer and friction characteristics.

To enhance the forced convection inside a passive heat exchanger tube, two different methods are typically used. One method is to alter the flow by changing the inner geometry of the tube. Another method is to insert loose or fastened geometrical inserts filling the cross-section of the tube, thereby promoting mixing resulting in enhanced heat transfer. These techniques do in general increase the pressure loss as well, which results in the best geometry having an optimal combination of increased heat transfer at slightly higher pressure loss. As a result, numerous studies have already been carried out to investigate the effect of both spirally and transversely tube corrugation. Ganeshan and Rao [1] investigated the effect of Prandtl number in seven different spirally corrugated tubes having different width and height of corrugation while suggesting the ratio between heat exchanger capacity to pumping power to be 100 to 150 % more efficient for Pr = 4.3 than for Pr = 109. As a result, this study suggests the spirally corrugated tubes to be attractive especially for fairly viscous fluids with high Prandtl numbers.

Zimparov et al. [2] conducted experiments on 25 spirally corrugated tubes having pitch heights e/D in the range 0.017 to 0.046 and pitch length in the range 0.25 to 0.65. The study found heat transfer enhancement factors ranging from 1.77 to 2.73 while the friction factor was increased from 100 to 400 %.

While most studies focus on the region unaffected by

*Corresponding author: Tel.: +45 22 50 81 31

Email address: jah@et.aau.dk (J. Hærvig)

entrance effects, Rainieri and Pagliarini [3] investigated entrance for highly viscous fluids with Reynolds number ($90 <$ Re < 800) using experiments and found that even a high swirl component does not always result in enhanced heat transfer for $200 <$ Re < 800.

The number of studies on corrugated tubes of different shapes are increasing in literature. They range from twisted square ducts (Bhadouriya et al. [4]), twisted oval tubes (Tan et al. [5]), sinusoidal transversely corrugated tubes (Zheng et al. [6]), to more commonly reported corrugated tubes of different shapes. Ağra et al. [7] does a numerical study on two corrugated and two helically finned tubes and while concluding that the helically finned tubes generally have better heat transfer and higher pressure loss, more studies should be carried out on a wider range of geometrical parameters to investigate the detailed flow. Han et al. [8] investigated convex corrugated tubes using 2D axisymmetric CFD simulations. The study concluded that asymmetric corrugated tubes exhibit an increased heat transfer performance of 8-18% compared to symmetric corrugated tubes. Mohammed et al. [9] reported integral values of heat transfer and pressure loss for tubes categorised by pitch height, rib height and rib width. The study concluded that of the geometries investigated, the highest Nusselt number was obtained for the highest height and width and lowest pitch. Han et al. [10] investigated opposite flow directions in the same corrugated tubes and found that the larger corrugation radius should be located in the upstream direction for corrugations described by two corrugation radii.

The more recent study by Vicente et al. [11] presents a systematic investigation where both the Reynolds and Prandtl numbers are varied from 2000 to 90,000 and 2.9 to 92 respectively for ten different corrugated tubes. Furthermore, the study gives an overview of different correlations presented in literature and concludes that for the same corrugation type, the published results deviate by a factor of 1.3 to 3 in friction factor augmentation and between 1.2 to 2 for Nusselt number augmentation. Likewise, the literature overview by Kareem et al. [12] gives a great overview of all the studies published in the period 1977 to 2015. The study clearly shows that the number of publications on passive heat transfer enhancement has increased in recent years, which is attributed an increased awareness of energy savings. Furthermore, the study concludes that even though quite a number of studies already have been published, more parameters should be investigated to cover larger design spaces.

While a large number of experimental studies on different spirally corrugated tubes have been carried out, more detailed studies on the flow field in various corrugations are limited. This study presents a systematic approach where geometrical changes are made to the sinusoidally, corrugated tube by varying the corrugation height and length. Furthermore, the effects of changing the geometry are quantified by comparing to non-dimensional maps for heat transfer and pressure loss.

2. Geometry and Parameters of Interest

2.1. Terminology and Representation of the Geometry

The geometry in this study is fully described by two parameters; a corrugation height and a corrugation length. Depending on the type of corrugated tube, different sets of dimensionless numbers are typically used to describe the geometry. For sinusoidally corrugated tube investigated in this study, the geometry is fully described by two numbers; a corrugation height and length defined as:

1. Corrugation length p: the corrugation length being the stream-wise distance between two successive points where the geometry repeats itself.
2. Corrugation height e: the corrugation height being the constant distance between the surface of corrugated tube and the non-corrugated tube with same diameter.

While including a lot of parameters defining the corrugations, numerous studies have shown that two main parameters are required to describe the performance; namely corrugation height and length. The purpose of this study is therefore to vary these parameters widely. To make the results applicable to any size of corrugated tube, the rest of the study reports corrugation heights and lengths made non-dimensional with the tube diameter, forming Π_1 and Π_2:

$$\Pi_1 = p/D \tag{1}$$
$$\Pi_2 = e/D \tag{2}$$

The tubes in this study differ from other studies by having a perfect circular cross-section. Corrugation is therefore introduced by having a centre line that twists in the stream-wise direction. The centre line section for one repeatable part of heat exchanger geometry is described by the sinusoidal function in (3) for $t \in [0; 1]$:

$$\begin{aligned} x(t) &= e \cdot \sin(2\pi t) \\ y(t) &= e \cdot \cos(2\pi t) \\ z(t) &= p \cdot t \end{aligned} \tag{3}$$

Based on the parametric representation in (3), the geometries will take the form shown in Fig. 1.

2.2. Normalisation and performance parameters

The quantities reported in this study are all made non-dimensional. All velocities are normalised by the stream-wise bulk velocity u_{b} and all temperatures by the bulk temperature T_{b}. The bulk velocity is based on the stream-wise velocity component z of the velocity field. The bulk velocity and temperature at position z along the tube length are defined as:

$$u_{\mathrm{b}}(z) = \frac{1}{A} \int \int u_{\mathrm{z}}(z, r, \theta) \, \mathrm{d}r \mathrm{d}\theta \tag{4}$$

$$T_{\mathrm{b}}(z) = \frac{1}{A} \int \int \frac{T(z, r, \theta) \, u(z, r, \theta)}{u_{\mathrm{b}}(z)} \mathrm{d}r \mathrm{d}\theta \tag{5}$$
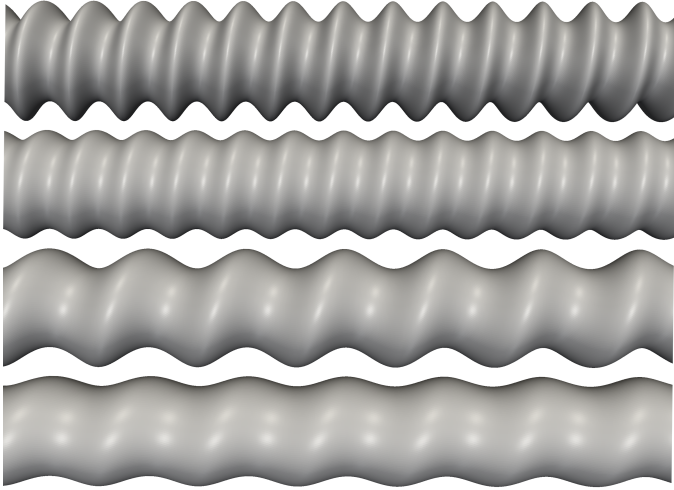
Figure 1: Examples of spirally corrugated tubes having different corrugations. From top to bottom: Tube 1: $p/D = 0.5$, $e/D = 0.10$; Tube 2: $p/D = 0.5$, $e/D = 0.05$; Tube 3: $p/D = 1.0$, $e/D = 0.10$; Tube 4: $p/D = 1.0$, $e/D = 0.05$.

Where A denotes the cross-sectional area of the tube. To report flow velocities, the Reynolds number based on the bulk velocity is used. To evaluate and compare the performance of the different corrugated tubes, two dimensionless quantities describing the heat transfer and pressure loss are used. In the case of corrugated tubes, two distinct different phenomena contributed to the pressure loss; wall shear stresses related to the local velocity gradients normal to the tube surface, and pressure drag related to the local pressure distribution along the surface. By integrating the two over the surface and averaging yields a single friction factor parameter that takes both into account and is a direct measure of the pressure loss in the tube. The Darcy-Weisbach friction factor describing pressure loss and Nusselt number describing heat transfer are defined as:

$$f = \Delta p \frac{2}{\rho u_b^2} \frac{D}{p} \tag{6}$$

$$\mathrm{Nu} = \frac{hD}{k} \tag{7}$$

where δp is the pressure loss over the periodic section with stream-wise length p. To evaluate the performance of the corrugated tubes, numerous criteria have been proposed in studies by Bergles et al. [13] and Webb [14]. In this study, the purpose is to increase heat transfer performance while maintaining the same pumping power power. In the case of constant inlet temperature and no additional thermal resistances due to for example fouling, Webb [14] suggests the criterion given by eq. (8) for constant Re and Pr. This criterion has been used in numerous studies to evaluate changes in heat exchanger geometries [10], [15]:

$$\eta = \frac{\mathrm{Nu}/\mathrm{Nu_s}}{(f/f_s)^{1/3}} \tag{8}$$

where subscript s denotes non-corrugated tubes ($e/D = 0$). As reference for the non-corrugated tubes, the widely accepted correlations for the straight tube suggested by Gnielinski [16] and Filonenko [17] are used:

$$\mathrm{Nu_s} = \frac{(f_s/8)\,(\mathrm{Re} - 1000)\,\mathrm{Pr}}{1 + 12.7\sqrt{(f_s/8)}\left(\mathrm{Pr}^{\frac{2}{3}} - 1\right)} \left[1 + \left(\frac{D}{L}\right)^{\frac{2}{3}}\right] K \tag{9}$$

$$f_s = (1.8\,\log_{10}\mathrm{Re} - 1.5)^{-2} \tag{10}$$

where tube diameter to total pipe length ratio D/L takes entrance effects into account. In this study where the fully-developed flow is investigated by using stream-wise periodicity, this term equals zero. The correction factor K used for this study is $(T_b/T_w)^n$ with n being 0.45 as discussed by Hufschmidt and Burck [18] and Jakovlev [19].

3. Numerical Setup

3.1. Governing equations

The governing equations being solved are the URANS (Unsteady Reynolds-averaged Navier-Stokes) equations. That is, the continuity (11) and momentum (12) equations are solved respectively:

$$\frac{\partial \bar{u}_i}{\partial x_i} = 0 \tag{11}$$

$$\frac{\partial \bar{u}_i}{\partial t} + \frac{\partial (\bar{u}_i \bar{u}_j)}{\partial x_j} = -\frac{1}{\rho}\frac{\partial \bar{p}}{\partial x_i} + \frac{\partial}{\partial x_j}\left((\nu + \nu_t)\frac{\partial \bar{u}_i}{\partial x_j}\right) + \beta\delta_{3,i} \tag{12}$$

where the last term in equation (12) is added to account for the pressure loss in the periodic domain using the in-built function in ANSYS Fluent. The β term is found by iteration in Fluent to account for the pressure loss over the small periodic section being modelled. To make the temperature field periodic, the periodic heat transfer model in Fluent is used where equation (13) is being solved:

$$\frac{\partial \theta}{\partial t} + \frac{\partial \bar{u}_j \theta}{\partial x_j} = \frac{\partial}{\partial x_j}\left(\frac{\partial \theta}{\partial x_j}\left(\frac{\nu}{\mathrm{Pr}} + \frac{\nu_t}{\mathrm{Pr_t}}\right)\right) \tag{13}$$

where the eddy-viscosity ν_t is the additional viscosity due to the turbulent scales being modelled using the URANS approach. In this study, the transition SST turbulence model is used to model turbulence. The transition SST turbulence model combines transition modelling by Menter et al. [20] and the standard SST model by Menter [21]. Using the transition SST turbulence model, the boundary layer separation downstream a corrugation is more accurately predicted. The following explains the momentum source term $\beta\delta_{3,i}$ and the scaled temperature field θ.

3.1.1. Stream-wise periodicity

As the flow in the majority of the heat exchanger tubes is both hydro-dynamically and thermally fully developed, focus will be on this part of the heat exchanger. Instead of simulating the whole heat exchanger starting with a non-developed flow and dealing with how the flow develops hydro-dynamically and thermally, periodic boundaries are utilised to couple the inlet and outlet. Using this approach, the inlet and outlet are two-way coupled and therefore a driving force is required to balance out the pressure loss to keep the fluid flowing. Likewise, modifications are required to keep the temperature from asymptotically approaching the wall temperature. All turbulent properties used for SST transition turbulence modelling are made periodic as well, so that the values at the inlet and outlet boundaries are obtained as the simulation converges. Therefore all boundary values at the periodic inlet and outlet are obtained during convergence. The approach suggested by Patankar et al. [22] is used to make both the temperature and pressure field repeat itself in a periodic manner. Therefore the $\beta\delta_{3,i}$ term is added to eq. (12) to make the pressure and velocity field periodic. When using this approach, only the computational domain shown in Fig. 2 is used.
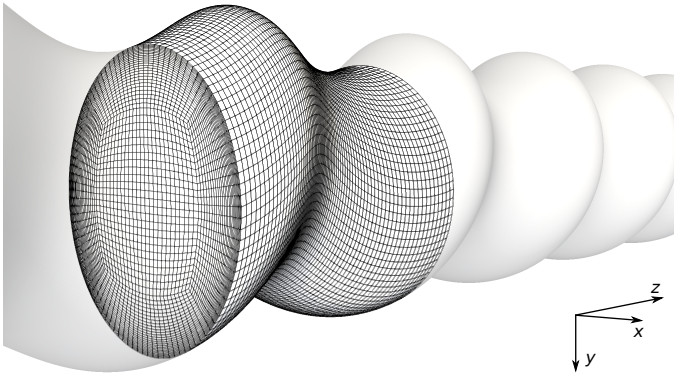

Figure 2: Overview of the computational mesh and the stream-wise periodic boundaries used.

Assuming a constant wall temperature, the fully-developed temperature field is obtained by solving for the scaled temperature field θ as suggested by Patankar et al. [22]:

$$\theta(x,y,z) = \frac{T(x,y,z) - T_{\mathrm{w}}}{T_z{}^* - T_{\mathrm{w}}} \qquad (14)$$

where $T(x,y,z)$ is the temperature field, T_{w} is the constant wall temperature, and $T_z{}^*$ is a local reference temperature profile at the inlet. The reference temperature $T_z{}^*$ at stream-wise position z is given by the following integral over the cross-sectional surface A:

$$T_z{}^* = \frac{\int_A T|\rho\vec{u}\cdot\mathrm{d}\vec{A}|}{\int_A |\rho\vec{u}\cdot\mathrm{d}\vec{A}|} \qquad (15)$$

That is, solving eq. (14) yields the stream-wise periodic temperature profile, which is used directly to evaluate the local heat transfer coefficient and consequently Nusselt numbers.

3.2. Numerical procedures

Simulations are carried out using the commercial AN-SYS Fluent 16.2 software. The governing equations are discretised using the finite volume method. The pressure and temperature equations are discretised using a 2nd order schemes, while the momentum equation is discretised using a 2nd order upwind scheme. Turbulent kinetic energy, specific dissipation rate, intermittency, and momentum thickness Reynolds number are all solved using 1st order upwind scheme. The transient term is discretised using a 1st order implicit formulation. To couple the velocity and pressure fields, the SIMPLE algorithm is used.

3.3. Mesh Topology

Structured meshes consisting of hexahedral elements are formed using the meshing tool blockMesh. A quarter of the cross-sectional mesh is shown in Fig. 3 while the overall mesh is visualised in Fig. 2.
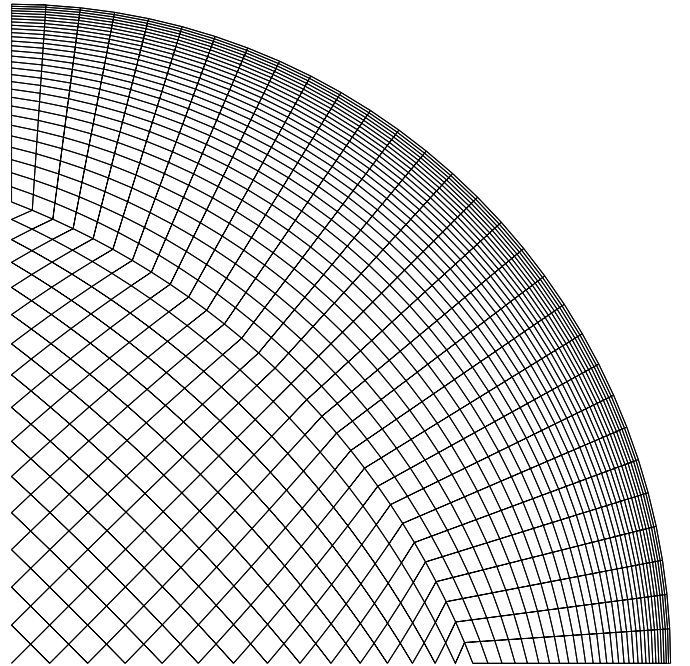

Figure 3: Overview of the computational mesh visualised by a quarter of the cross-sectional mesh.

The cross-sectional mesh is extruded along the path described by (3) resulting in a structured mesh having the same cross-sectional mesh along the length of the tube. The first cell normal to the wall is placed at $y^+ \approx 1$ to resolve the viscous sub-layer part of the boundary layer. Fig. 4 and 5 shows the quality of the mesh in terms of

4

cell angles defined by orthogonal quality and equiangular skew quality defined as:

$$\text{Equiangular skew} = \max\left[\frac{\theta_{\max} - \theta_{\mathrm{e}}}{180° - \theta_{\mathrm{e}}}, \frac{\theta_{\mathrm{e}} - \theta_{\min}}{\theta_{\mathrm{e}}}\right] \quad (16)$$

$$\text{Orthogonal quality} = \min\left[\frac{\boldsymbol{A} \cdot \boldsymbol{f}}{|\boldsymbol{A}||\boldsymbol{f}|}, \frac{\boldsymbol{A} \cdot \boldsymbol{c}}{|\boldsymbol{A}||\boldsymbol{c}|}\right] \quad (17)$$

where $\theta_{\mathrm{e}} = 90°$ for the hexahedral elements in this study. In (17), $\boldsymbol{A}$ is a face cell normal vector, $\boldsymbol{f}$ is vector from the cell centroid to the face centroid and $\boldsymbol{c}$ is a vector between two adjacent cell centroids.
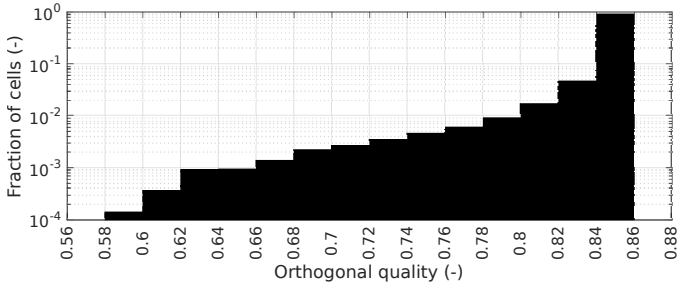

Figure 4: Overview of orthogonal quality for the mesh.
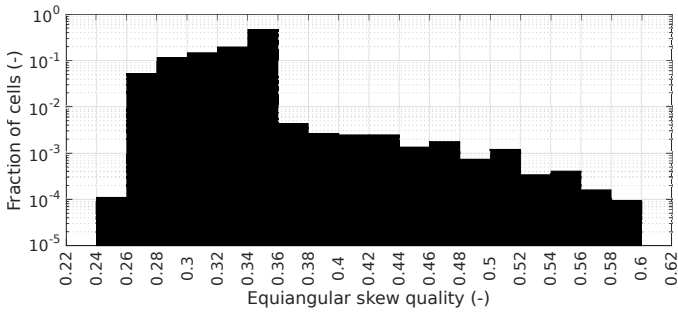

Figure 5: Overview of equiangular skew quality for the mesh.

As shown in Fig. 4 and 5, 90.4% of the cells have a high orthogonal quality above 0.84 and 98.2% have an equiangular skew quality below 0.36. The first boundary layer cells have a maximum aspect ratio of 24.

3.4. Validation of Results

To ensure the results reported in this study are reliable, two measures are taken. First, the number of cells is approximately doubled until the results are well within the asymptotic range and close to the estimated true numerical value. For all meshes, the first cell height is placed within the viscous sub-layer at $y^+ \approx 1$ so that the transition SST turbulence model is applicable. Fig. 6 shows the grid convergence study in terms of average Nusselt number.
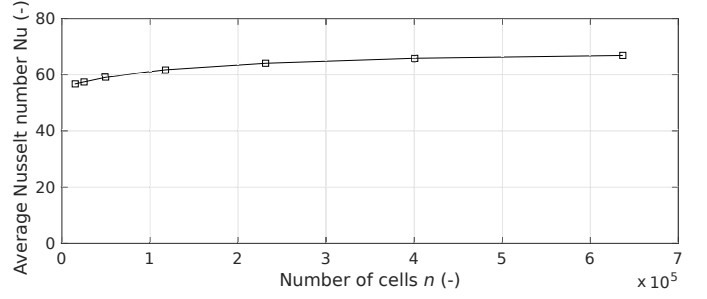

Figure 6: Grid independence study to investigate the importance of cell count for a corrugated pipe ($\Pi_1 = 1$ and $\Pi_2 = 0.1$).

To estimate the numerical error, Richardson extrapolation is used as suggested by Roache [23]. To check whether the different meshes are within the asymptotic range of the true numerical value for zero grid spacing, the order of convergence p is estimated as:

$$p = \frac{\ln\left[\frac{f_3 - f_2}{f_2 - f_1}\right]}{\ln(r)} \quad (18)$$

where f_1, f_2 and f_3 refer to values obtained by the finest, second finest and third finest grids respectively while r refers to grid refinement ratio between two successive grid refinements. Using Richardson extrapolation, the true value at zero grid spacing f_0 is estimated as [23]:

$$f_0 \approx f_1 + \frac{f_1 - f_2}{p^r - 1} \quad (19)$$

To estimated the required grid resolution, the grid convergence index (GCI) proposed by Roache [23] is used:

$$\text{GCI}_{\mathrm{n}} = \frac{F_{\mathrm{s}}|\epsilon|}{r^p - 1} \quad (20)$$

where F_{s} is a safety factor, ϵ is the relative error between two grids $\epsilon = (f_{\mathrm{n}} - f_{\mathrm{n}+1})/f_{\mathrm{n}}$. Using a safety factor of 3.0, grid refinement factors $\text{GCI}_{12} = 0.037$ and $\text{GCI}_{23} = 0.067$ are obtained. In this study, the Nusselt number obtained by the mesh having 400,500 cells is within the error band $\text{Nu}_0 \pm \text{Nu}_0 \cdot \text{GCI}_{12}$ and therefore the mesh having 400,500 cells is used for the rest of the simulations.

The results obtained for a straight tube ($\Pi_1 = 1$, $\Pi_2 = 0$) are in Fig. 7 and 8 compared to eq. (9) and (10) by Gnielinski [16] and Filonenko [17] for various Reynolds and Prandtl numbers.
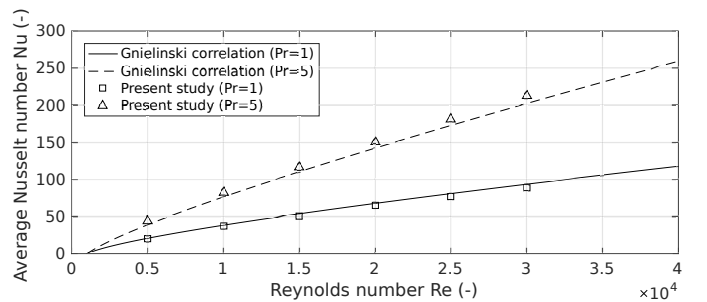

Figure 7: Comparison to the Gnielinski correlation ($\Pi_1 = 1$ and $\Pi_2 = 0$).
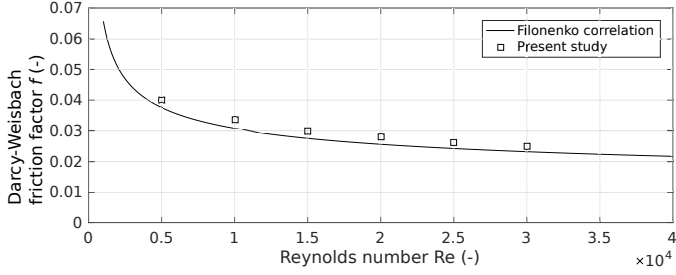
5

Figure 8: Comparison to the Filonenko correlation ($\Pi_1 = 1$ and $\Pi_2 = 0$).

The comparison suggests the CFD simulations to be able to predict smooth pipe performance. For the results in Fig. 7 and 8, the Nusselt numbers and friction factors numbers are within a maximum deviation of 5.4 % and 8.6 % respectively.

4. Detailed Flow Field

To understand the mechanisms governing heat transfer and pressure loss, the flow is visualised in a wide range of geometrically different corrugated tubes. The flow fields are plotted in the representative periodic region shown with black in Fig. 9.
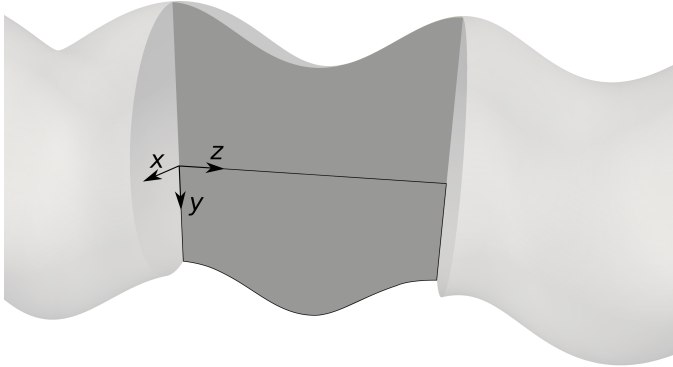

Figure 9: Region outlined with black is used for visualisation of the flow field. Note the upper half shows the exact same flow field but is shifted half a period.

The region outlined in Fig. 9 gives a complete overview of the three-dimensional fully-developed flow field. That is, all quantities of interest such as velocity, pressure and temperature at $z = 0$ for positive y-values are the same at $z = D \cdot \Pi_1/2$ (middle of periodic section) for negative y-values.

To generalise the observations, all quantities of interest are reported in dimensionless quantities. The position in the tube is made non-dimensional by the tube diameter D. The static pressure in the tube is reported using the pressure coefficient C_p, which is the ratio between static pressure and the dynamic pressure based on the bulk velocity in:

$$C_p(x, y, z) = \frac{p(x, y, z) - p_\infty}{\frac{1}{2}\rho u_b^2} \qquad (21)$$

Where the free stream pressure p_∞ is taken at the centre of the tube at $(x, y, z) = (0, 0, 0)$. The swirling flow is quantified by the ratio of absolute tangential velocity $|u_{\text{tan}}|$ to bulk velocity u_b:

$$\psi(x, y, z) = \frac{|u_{\text{tan}}(x, y, z)|}{u_b(z)} \qquad (22)$$

Using this ratio, $\psi = 0$ corresponds to a purely axial flow, while values $\phi \geq 1$ shows regions where the tangential velocity locally exceeds the local axial flow. To quantify the re-circulation zones, a re-circulation factor is defined as the ratio of stream-wise velocity u_z to bulk velocity:

$$\phi(x, y, z) = \frac{u_z(x, y, z)}{u_b(z)} \qquad (23)$$

Using this dimensionless number, re-circulation zones are visualised as having $\phi < 0$. In the following section, the corrugation height and length are varied and the corresponding changes in flow fields are reported using the above mentioned dimensionless numbers.

4.1. Effect of corrugation height on the flow field

In the following, changes in flow field caused by varying corrugation height from $e/D = 0.01$ to $e/D = 0.16$ are reported.

4.1.1. Pressure field

Fig. 10 to 13 show how changes in corrugation height affects the pressure field visualised by pressure coefficient given by (21).
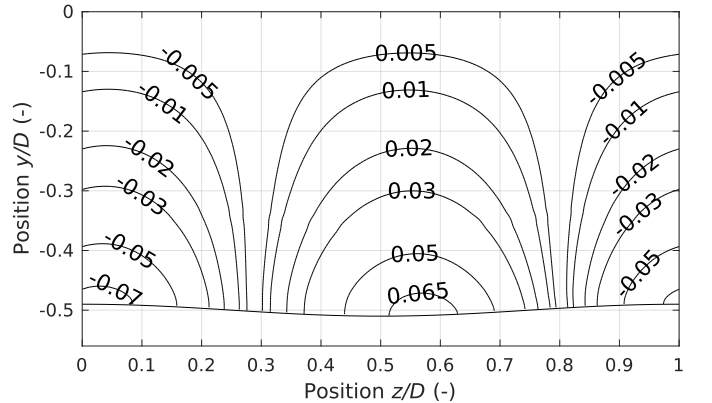

Figure 10: Pressure field visualised by the pressure coefficient $C_p = (p - p_\infty) / (1/2\rho u_b^2)$ in a corrugated tube with corrugation height and length of $e/D = 0.01$ and $p/D = 1.0$ respectively at $Re = 10,000$.
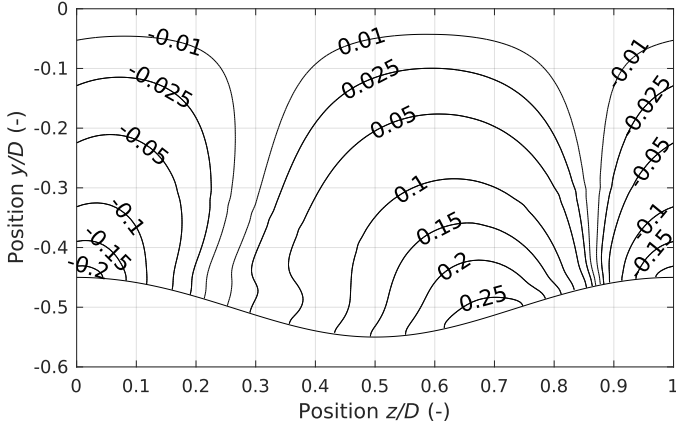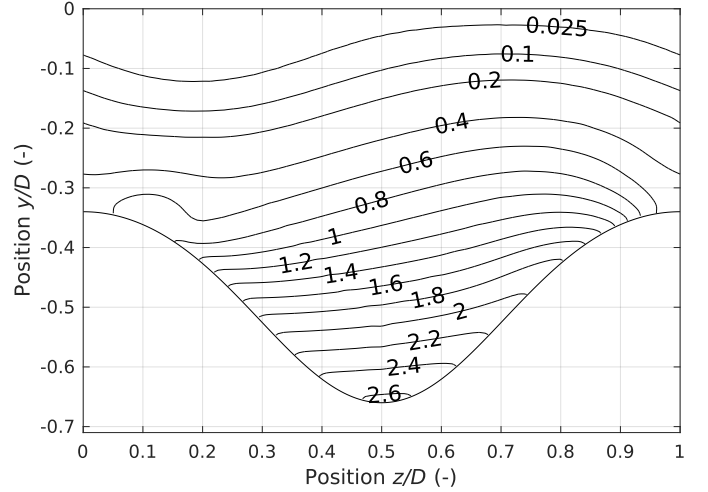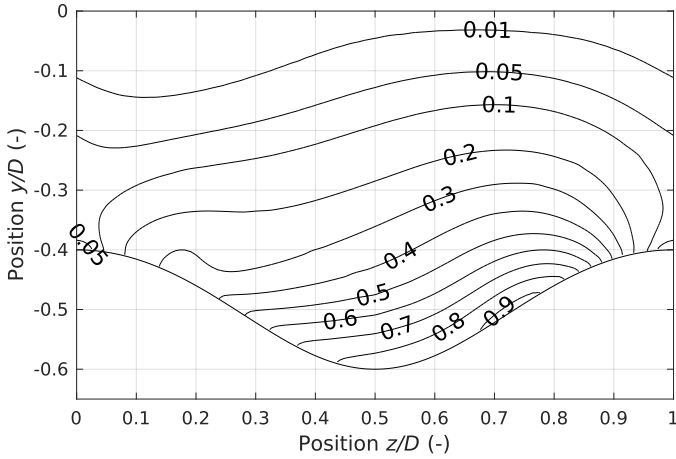
Figure 11: Pressure field visualised by the pressure coefficient $C_\mathrm{p} = (p - p_\infty) / \left(1/2\rho u_\mathrm{b}^2\right)$ in a corrugated tube with corrugation height and length of $e/D = 0.05$ and $p/D = 1.0$ respectively at $\mathrm{Re} = 10{,}000$.

Figure 13: Pressure field visualised by the pressure coefficient $C_\mathrm{p} = (p - p_\infty) / \left(1/2\rho u_\mathrm{b}^2\right)$ in a corrugated tube with corrugation height and length of $e/D = 0.16$ and $p/D = 1.0$ respectively at $\mathrm{Re} = 10{,}000$.

Figure 12: Pressure field visualised by the pressure coefficient $C_\mathrm{p} = (p - p_\infty) / \left(1/2\rho u_\mathrm{b}^2\right)$ in a corrugated tube with corrugation height and length of $e/D = 0.10$ and $p/D = 1.0$ respectively at $\mathrm{Re} = 10{,}000$.

At a low corrugation $e/D = 0.01$, the point of maximum pressure is located close to the centre of corrugation $z/D \approx 0.55$ but with low pressure coefficients $C_\mathrm{p} < 0.1$. At a slightly higher corrugation height of $e/D = 0.05$, the point of highest pressure coefficient is moved further downstream to $z/D \approx 0.7$, while the pressure coefficient is increased to 0.25. At both $e/D = 0.01$ and $e/D = 0.05$, the pressure contours are orientated normal to the stream-wise direction. Increasing the corrugation height to $e/D = 0.10$ results in the point of highest pressure coefficient to move further downstream to $z/D \approx 0.75$, while pressure contours changes direction to be mostly stream-wise oriented revealing a significant swirl component, which is described below. At a extreme corrugation height of $e/D = 0.16$, the point of highest pressure coefficient is moved upstream again to the centre of corrugation $e/D = 0.5$ where the pressure coefficient obtains values $C_\mathrm{p} \geq 2.6$. To explain the sudden change in orientation of pressure coefficient contours from $e/D = 0.05$ to $e/D = 0.10$, the swirling flow fields are presented in the following.

4.1.2. Swirling flow field

Fig. 14 to 17 show how changes in corrugation height from $e/D = 0.01$ to $e/D = 0.16$ affect the flow field in terms of swirl defined by (22).
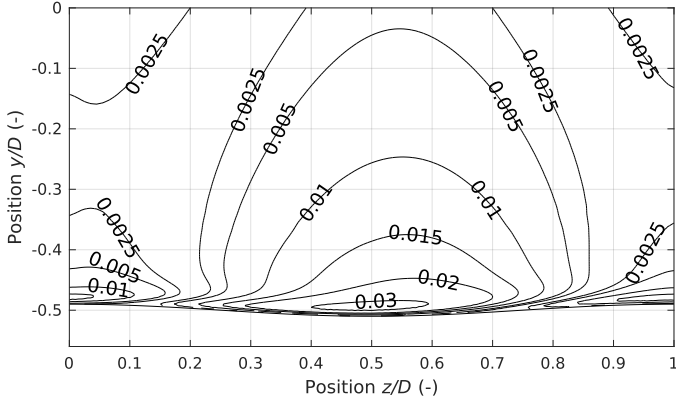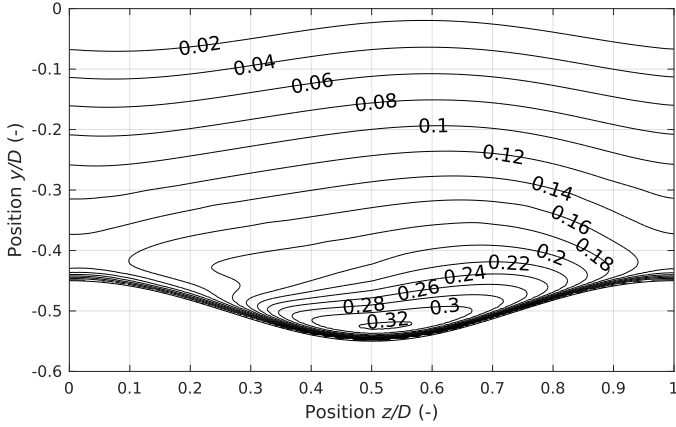
Figure 14: Swirling flow field visualised by contours of $\psi = |u_{\text{tan}}|/u_{\text{b}}$ in a corrugated tube with corrugation height and length of $e/D = 0.01$ and $p/D = 1.0$ respectively at Re = 10,000.

Figure 15: Swirling flow field visualised by contours of $\psi = |u_{\text{tan}}|/u_{\text{b}}$ in a corrugated tube with corrugation height and length of $e/D = 0.05$ and $p/D = 1.0$ respectively at Re = 10,000.
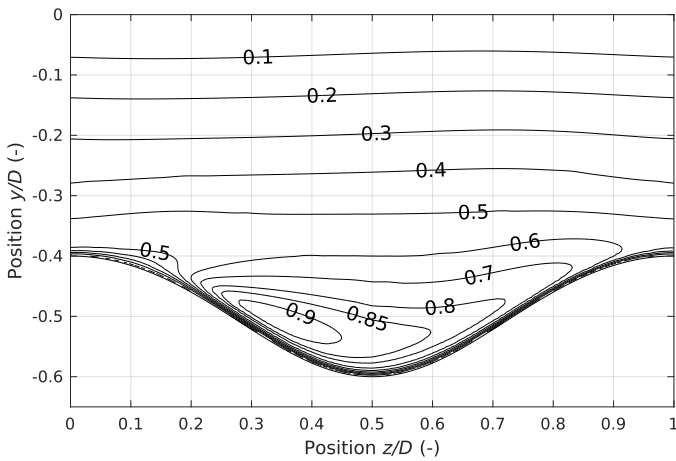

Figure 16: Swirling flow field visualised by contours of $\psi = |u_{\text{tan}}|/u_{\text{b}}$ in a corrugated tube with corrugation height and length of $e/D = 0.10$ and $p/D = 1.0$ respectively at Re = 10,000.
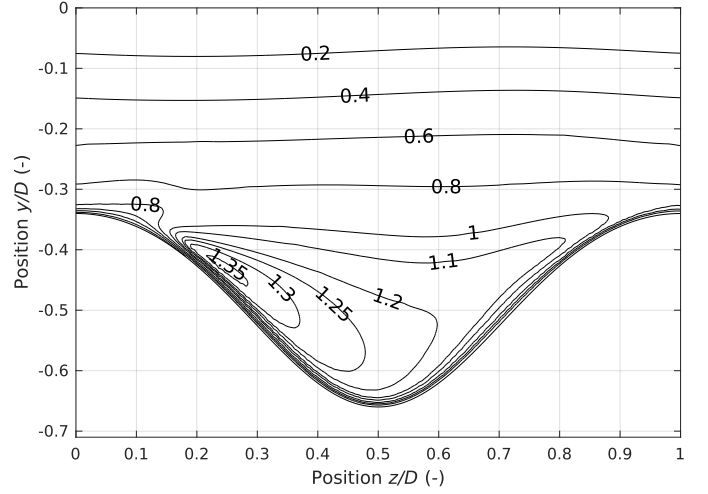

Figure 17: Swirling flow field visualised by contours of $\psi = |u_{\text{tan}}|/u_{\text{b}}$ in a corrugated tube with corrugation height and length of $e/D = 0.16$ and $p/D = 1.0$ respectively at Re = 10,000.

At a low corrugation height $e/D = 0.01$, there is an insignificant swirl which is maximum at the centre of corrugation at $z/D \approx 0.5$. Increasing the corrugation height from $e/D = 0.01$ to $e/D = 0.05$ causes the swirl to increase by a factor 10, while still being located close to the corrugation centre at $z/D \approx 0.5$. Introducing more severe corrugation heights of $e/D = 0.10$ and $e/D = 0.16$, increases the swirl while moving the point of maximum swirl upstream. At an extreme corrugation height of $e/D = 0.16$, the point of maximum swirl is located in the first part of the corrugated section at $z/D \approx 0.25$. Furthermore, at this corrugation height, swirl numbers above 1 suggests that the tangential velocity exceeds the bulk velocity in most of the corrugated section of the tube. The result is a flow field that differs significantly from the flow field in tubes having lower corrugation heights with insignificant swirl.

4.1.3. Re-circulating flow field

Fig. 18 to 21 show how changes in corrugation height from $e/D = 0.01$ to $e/D = 0.16$ affect the flow field in terms of re-circulating flow field defined by (23).
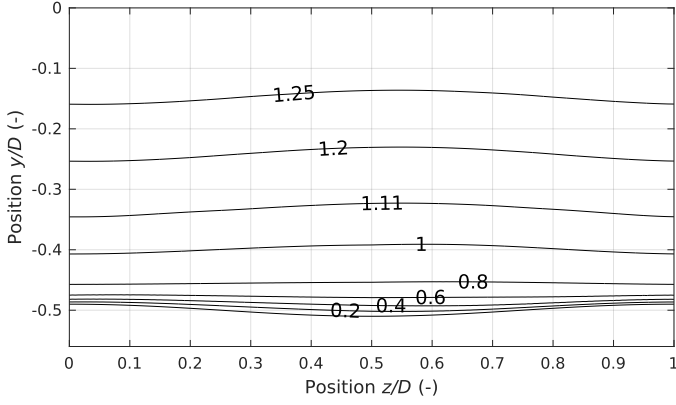
Figure 18: Re-circulation zones visualised by axial flow component normalised bulk velocity $u_{\text{axial}}/u_{\text{b}}$ in a corrugated tube with corrugation height and length of $e/D = 0.01$ and $p/D = 1.0$ respectively at Re = 10,000.

Figure 19: Re-circulation zones visualised by axial flow component normalised bulk velocity $u_{\text{axial}}/u_{\text{b}}$ in a corrugated tube with corrugation height and length of $e/D = 0.05$ and $p/D = 1.0$ respectively at Re = 10,000.
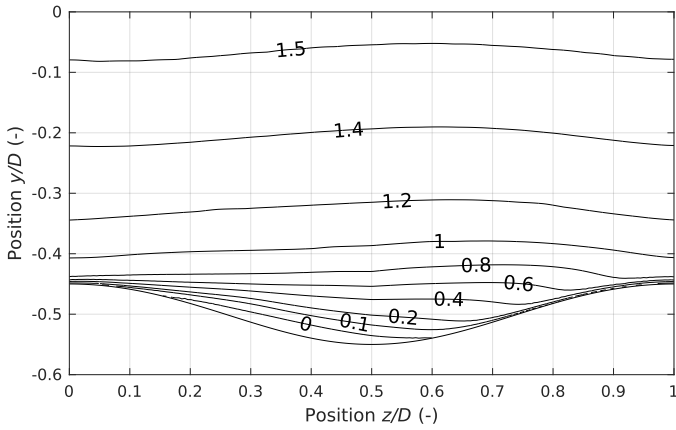

Figure 20: Re-circulation zones visualised by axial flow component normalised bulk velocity $u_{\text{axial}}/u_{\text{b}}$ in a corrugated tube with corrugation height and length of $e/D = 0.10$ and $p/D = 1.0$ respectively at Re = 10,000.
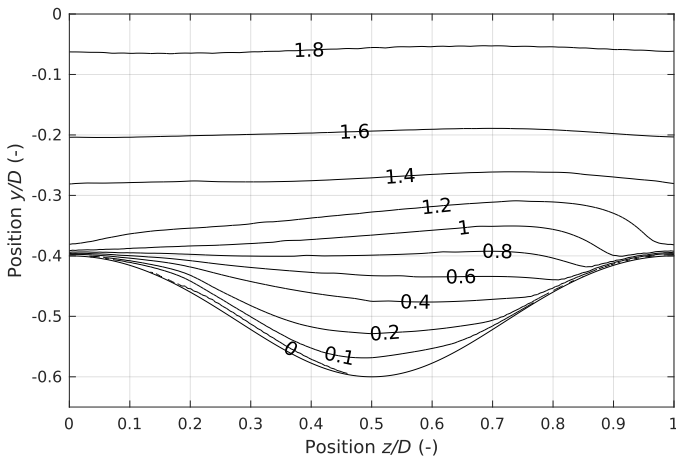

Figure 21: Re-circulation zones visualised by axial flow component normalised bulk velocity $u_{\text{axial}}/u_{\text{b}}$ in a corrugated tube with corrugation height and length of $e/D = 0.16$ and $p/D = 1.0$ respectively at Re = 10,000.

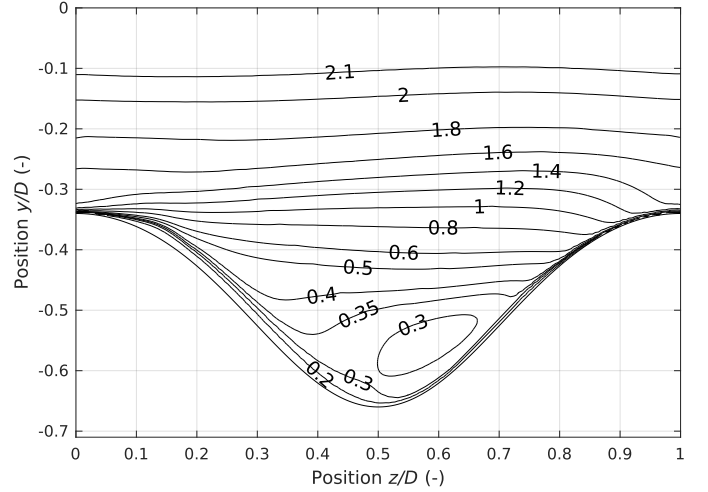At a low corrugations height of $e/D = 0.01$, the flow stay attached to the surface and no re-circulation zone is formed. At a slightly higher corrugation height of $e/D = 0.05$, the strong adverse pressure gradient causes the flow to separate and form a re-circulation zone in the first part of the corrugation section. At a higher corrugation height of $e/D = 0.10$ with a significantly higher swirl, the re-circulation zone is almost eliminated compared to the lower corrugation height of $e/D = 0.05$. That suggests the high swirl to suppress the re-circulation zone. At a even higher corrugation height of $e/D = 0.16$, the re-circulation zone is completely eliminated as a result of highest pressure being located at the centre of the corrugation as already shown in Fig. 13.

4.2. Effect of corrugation length on the flow field

In the following, changes in flow field as a result of varying the corrugation length from $p/D = 0.5$ to $p/D = 2.0$ are reported.

4.2.1. Pressure field

Fig. 22 to 24 shows how lowering and increasing the corrugation length from $p/D = 0.10$ affects the pressure field in the corrugated tubes. The case with $p/D = 0.10$ is already presented in Fig. 12. Increasing the corrugation length from $p/D = 0.5$ to $p/D = 1.5$ causes the the maximum pressure coefficient to increase (Fig. 22, 12 and 23). Furthermore, the location moves towards the centre of the corrugated section. Increasing the corrugation length further to $p/D = 2.0$, causes a slight decrease in maximum pressure coefficient. This can be explained by the tube approaching a non-corrugated tube as $p/D \to \infty$.

4.2.2. Swirling flow

Fig. 25 to 27 show how the swirling flow field is altered as the corrugation length is changed from a corrugation
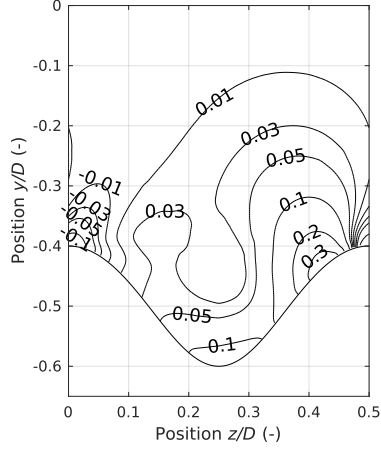
Figure 22: Pressure field visualised by the pressure coefficient $C_{\mathrm{p}} = (p - p_\infty) / \left(1/2\rho u_{\mathrm{b}}^2\right)$ in a corrugated tube with corrugation height and length of $e/D = 0.10$ and $p/D = 0.5$ respectively at Re $= 10,000$.

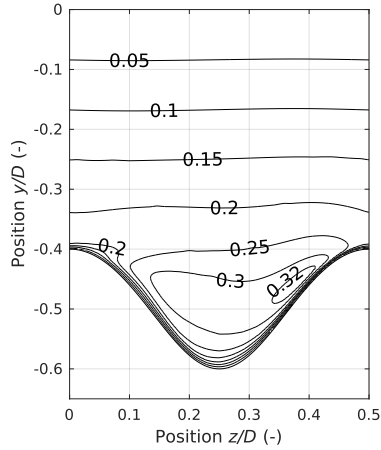length of $p/D = 1.0$ to $p/D = 0.5$, $p/D = 1.5$ and $p/D = 2.0$.

Figure 25: Swirling flow field visualised by contours of $\psi = |u_{\mathrm{tan}}|/u_{\mathrm{b}}$ in a corrugated tube with corrugation height and length of $e/D = 0.10$ and $p/D = 0.5$ respectively at Re $= 10,000$.

At a low corrugation length of $p/D = 0.5$, an almost swirl with almost constant magnitude is present in the corrugation section. When the corrugation length is increased from $p/D = 0.5$ to $p/D = 1.0$, the maximum swirl is increased from $\psi \approx 0.3$ to $\psi \approx 0.9$. With a further increase in corrugation length to $p/D = 1.5$, there is a minimal increase in swirl from $\psi \approx 0.9$ to $\psi \approx 0.95$, while the point of maximum swirl moves towards the centre of the corrugated section. Increasing the corrugation length further to $p/D = 2.0$ results in decrease in swirl. This can be explained by the fact that the corrugated tube approaching a non-corrugated tube as $p/D \to \infty$, where no swirl is present.

4.2.3. Re-circulating flow field

Fig. 28 to 30 show how the stream-wise flow field is altered as the corrugation length is changed from a corrugation length of $p/D = 1.0$ to $p/D = 0.5$, $p/D = 1.5$ and $p/D = 2.0$. Decreasing the corrugation length from $p/D = 1.0$ to $p/D = 0.5$ causes the flow to separate and form a large re-circulation zone filling up most of the corrugation section. This can be explained by significantly lower swirl velocity at the low corrugation length of $p/D = 0.5$ compared to $p/D = 1.0$. Increasing the corrugation length to $p/D = 1.5$ and $p/D = 2.0$ eliminates the re-circulation zone present at lower corrugations lengths of $p/D = 0.5$ and $p/D = 1.0$.

In the following section, the flow field presented in this section are linked to heat transfer and pressure loss characteristics.

5. Link Between Flow Field and Heat Exchanger Performance

Heat transfer and pressure loss are reported by the dimensionless Nusselt number defined by (7) and friction factor defined by (6). Fig. 31 and 32 show how changes in corrugation height and length affect the Nusselt number and Darcy-Weisbach friction factor.
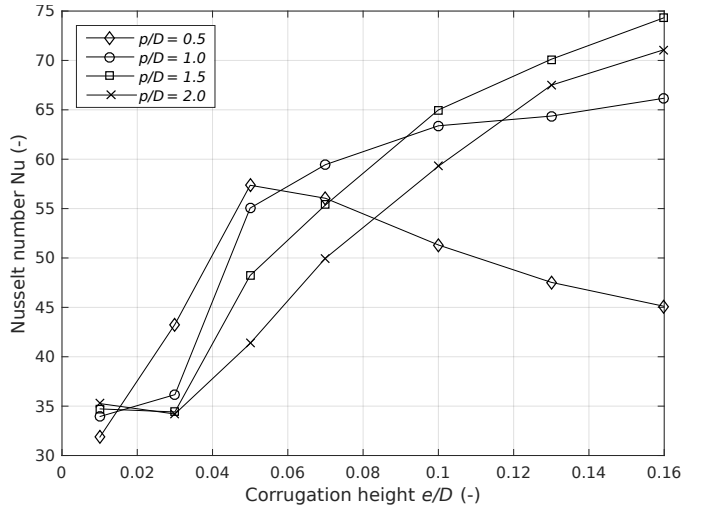

Figure 31: Nusselt number as function of dimensionless corrugation length p/D and height e/D at Re $= 10,000$ and Pr $= 1.0$.
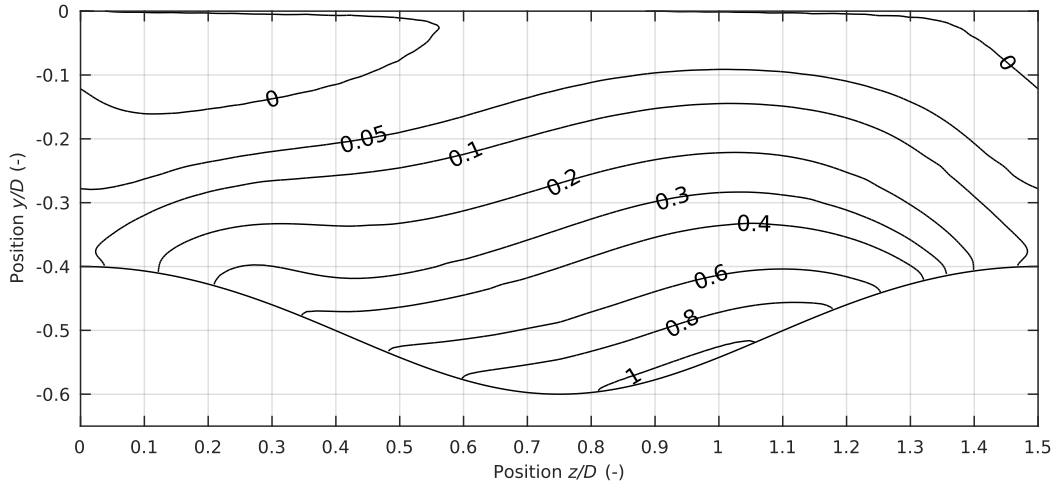
10

Figure 23: Pressure field visualised by the pressure coefficient $C_\mathrm{p} = (p - p_\infty) / \left(1/2\rho u_\mathrm{b}^2\right)$ in a corrugated tube with corrugation height and length of $e/D = 0.10$ and $p/D = 1.5$ respectively at $\mathrm{Re} = 10{,}000$.

Figure 24: Pressure field visualised by the pressure coefficient $C_\mathrm{p} = (p - p_\infty) / \left(1/2\rho u_\mathrm{b}^2\right)$ in a corrugated tube with corrugation height and length of $e/D = 0.10$ and $p/D = 2.0$ respectively at $\mathrm{Re} = 10{,}000$.
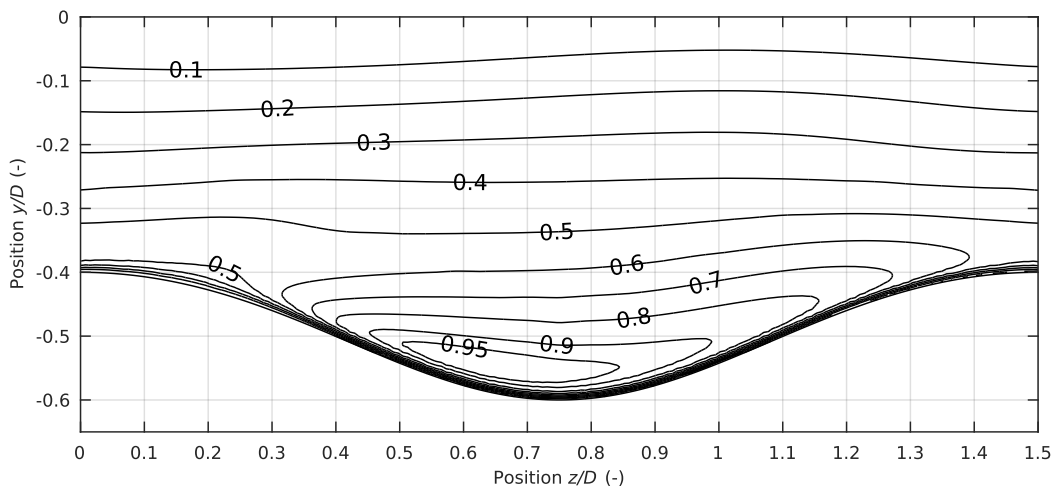
Figure 26: Swirling flow field visualised by contours of $\psi = |u_\mathrm{tan}|/u_\mathrm{b}$ in a corrugated tube with corrugation height and length of $e/D = 0.10$ and $p/D = 1.5$ respectively at $\mathrm{Re} = 10{,}000$.

11

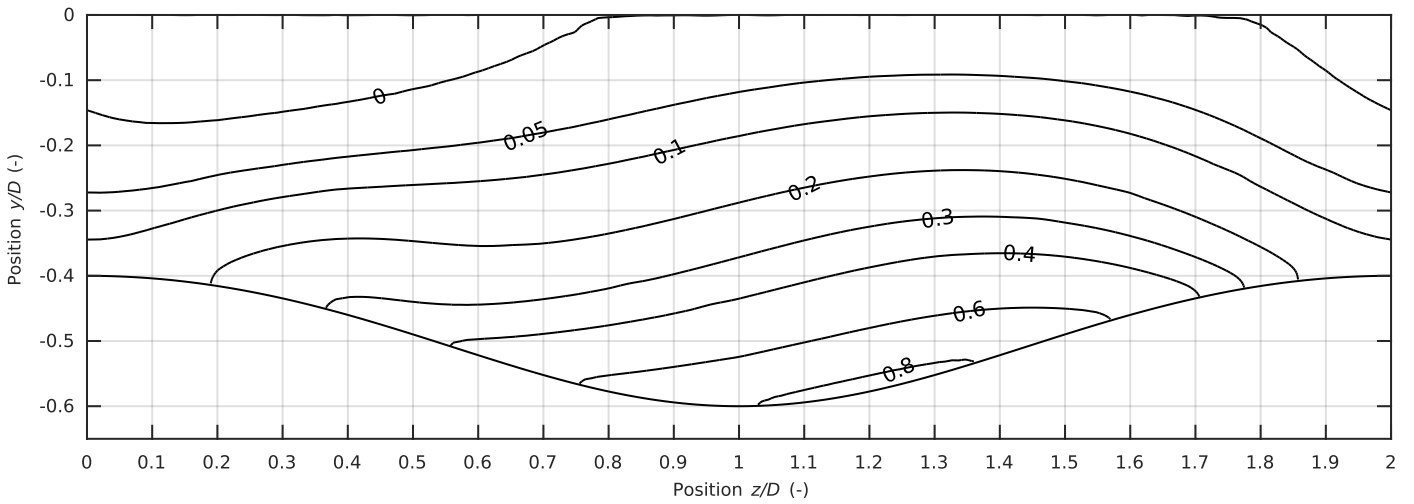Figure 27: Swirling flow field visualised by contours of $\psi = |u_{\mathrm{tan}}|/u_{\mathrm{b}}$ in a corrugated tube with corrugation height and length of $e/D = 0.10$ and $p/D = 2.0$ respectively at Re $= 10,000$.

Figure 28: Re-circulation zones visualised by axial flow component normalised bulk velocity $u_{\mathrm{axial}}/u_{\mathrm{b}}$ in a corrugated tube with corrugation height and length of $e/D = 0.10$ and $p/D = 0.5$ respectively at Re $= 10,000$.
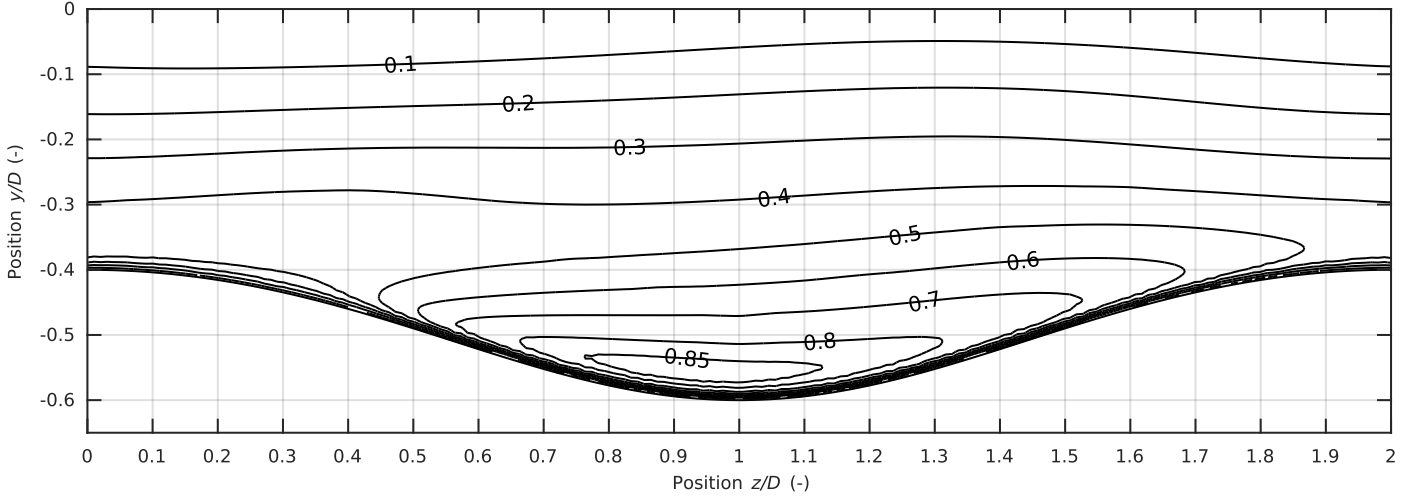

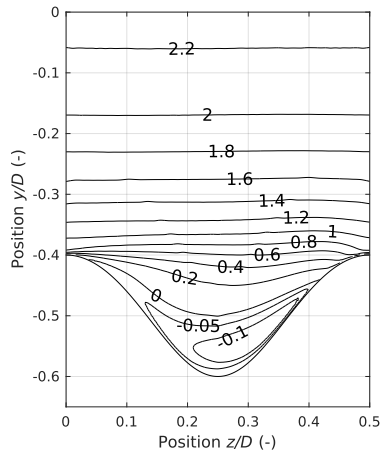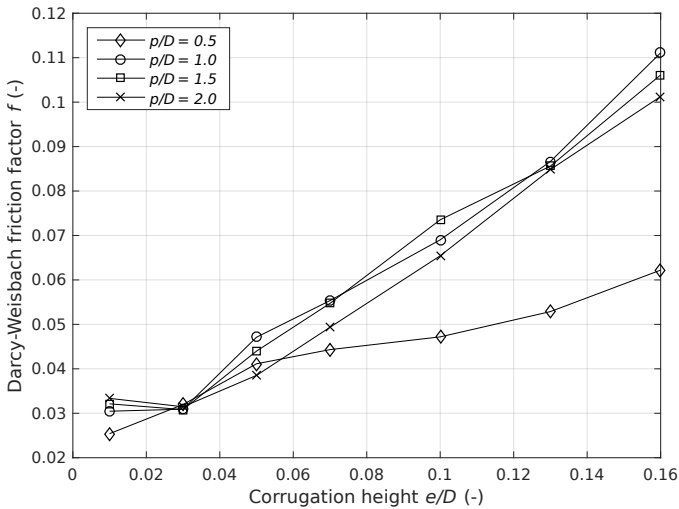Figure 32: Darcy-Weisbach friction factor as function of dimensionless corrugation length p/D and height e/D at Re $= 10,000$.

At sufficiently low corrugation heights $e/D = 0.01$, the performance in terms of Nusselt number approaches the non-corrugated tube as the flow fields are only affected to a minor degree. That is, the flow stay attached to the surface and only a small insignificant swirl is induced by the corrugation. At a slightly higher corrugation height $e/D = 0.05$, the Nusselt number is increased significantly. At this corrugation height, the flow separates and a higher swirl is induced. The result is an increased heat transfer at an increased pressure loss. At an even higher corrugation height, the swirl is increased even further and the swirling velocity eventually exceeds the stream-wise velocity. The result is steeper velocity gradients at the surface resulting in both higher heat transfer and pressure loss. When the corrugation height is increased beyond a certain point, the Nusselt number is expected to decrease as the heat transfer area increases without any additional increment in heat transfer. This point depends on the corrugation length. At a lower corrugation length $p/D = 0.5$, the decrease in Nusselt number happens between $e/D = 0.03$ and $e/D = 0.07$. At higher corrugation lengths $p/D = 1.0$, $p/D = 1.5$ and $p/D = 2.0$, the decrease in Nusselt number takes place at $e/D > 0.16$. At this point, a large re-circulation zone with low swirl velocities is present in the corrugation section. Here the flow is dominated by core flow with a high stream-wise velocity. Fig. 32 shows that the friction factor in general increases with corrugation height. However, the friction factor increases slower above the point where the Nusselt number begins to decrease.

To compare the various corrugated tubes at a constant pumping power and taking both Nusselt number and friction factor into account, the performance evaluation criterion given by (8) is used. This criterion is shown in Fig. 33 for the different corrugated tubes.
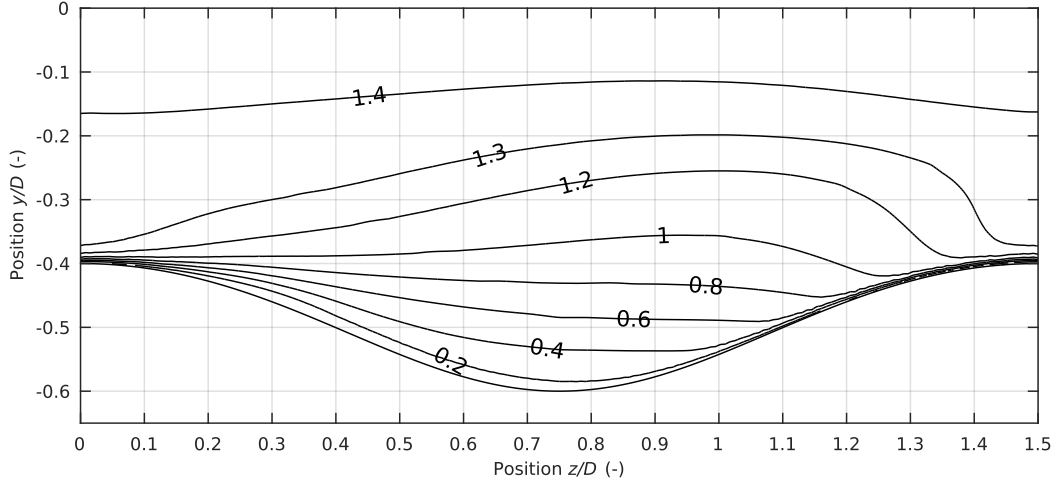
12

Figure 29: Re-circulation zones visualised by axial flow component normalised bulk velocity $u_{\mathrm{axial}}/u_{\mathrm{b}}$ in a corrugated tube with corrugation height and length of $e/D = 0.10$ and $p/D = 1.5$ respectively at $\mathrm{Re} = 10,000$.
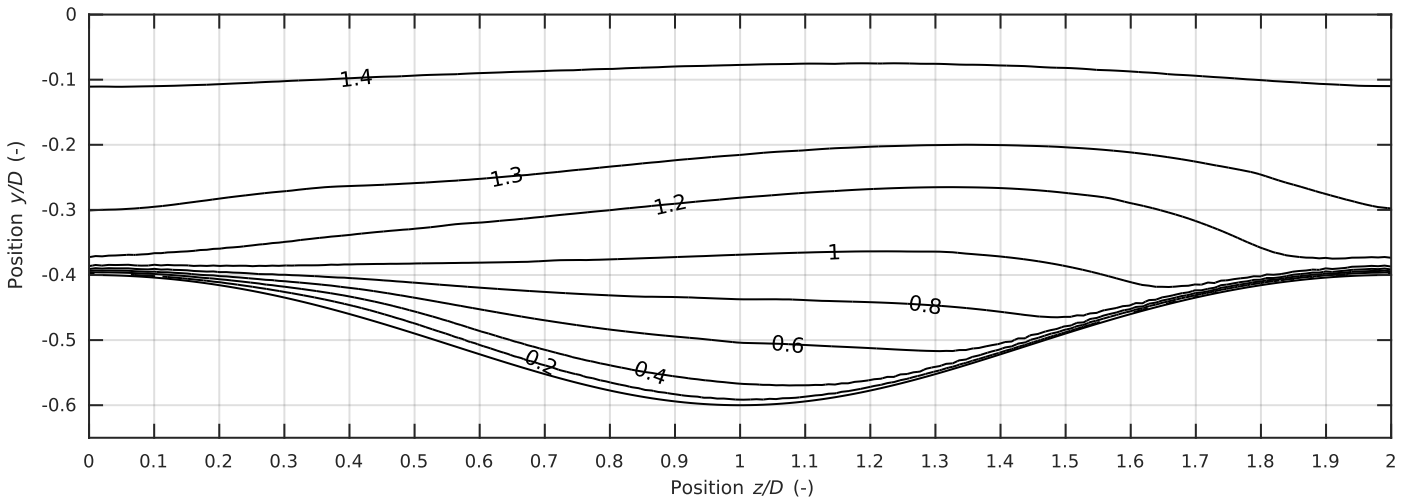

Figure 30: Re-circulation zones visualised by axial flow component normalised bulk velocity $u_{\mathrm{axial}}/u_{\mathrm{b}}$ in a corrugated tube with corrugation height and length of $e/D = 0.10$ and $p/D = 2.0$ respectively at $\mathrm{Re} = 10,000$.
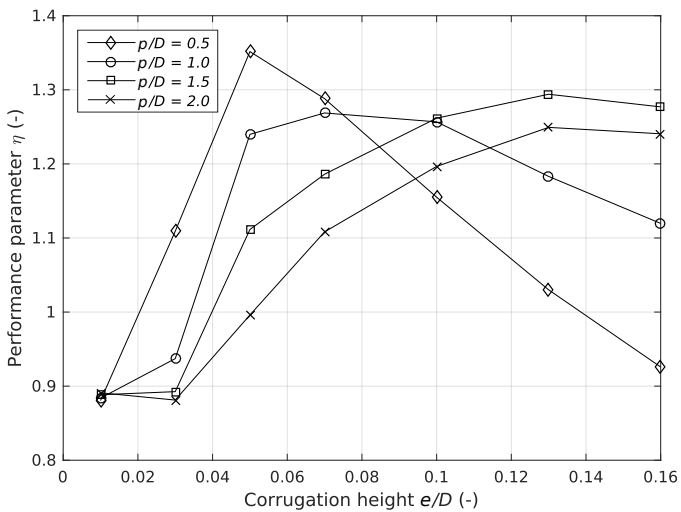

Figure 33: Performance parameter $\eta = (\mathrm{Nu}/\mathrm{Nu_s})/(f/f_{\mathrm{s}})^{1/3}$ as function of dimensionless corrugation length p/D and height e/D at $\mathrm{Re} = 10,000$ and $\mathrm{Pr} = 1.0$.

Fig. 33 shows that there is a corrugation height for every corrugation length that results in the highest performance parameter. For lower corrugation lengths, this point is found at lower corrugation heights. This optimum condition is explained by the fact that the friction factor continues to increase as the Nusselt number only increases slightly for $p/D = 1.0$, $p/D = 1.5$, and $p/D = 2.0$ or even decreases for $p/D = 0.5$.

6. Conclusion

In this study the fully-developed flow field in different sinusoidally, spirally corrugated tubes is investigated by computational fluid dynamics for a Reynolds number of 10,000 and Prandtl number of 1.0. The tubes have a constant cross-sectional area and corrugation is introduced by the tubes having a centre-line described by a sinusoidal function. The investigated corrugations have corrugations heights in the range 0 to 0.16 and corrugation lengths in

13

the range 0.5 to 2.0. The results suggests that sinusoidally, corrugated tubes of the sinusoidally, spirally type exhibit significant heat-transfer enhancing flow characteristics. To sum up, the major findings on how changes in corrugation height affects the flow field are:

- At low corrugations heights $e/D = 0.01$, the flow stay attached to the surface and only a small swirl is present with maximum at the centre of the corrugation.

- At slightly higher corrugations heights $e/D = 0.05$, the increased adverse pressure gradient causes the flow to separate resulting in a significant re-circulation zone. The swirling magnitude is increased again but is still centred at the corrugation centre.

- At a corrugation height $e/D = 0.10$, the swirling flow begins to dominate with tangential velocities in the order of the bulk velocity.

- At a high corrugation height $e/D = 0.16$, a strong swirl with a tangential velocity component exceeding the stream-wise velocity component is present in almost all the corrugation section. The high swirl eliminates re-circulation zones by a high pressure centred in the corrugation section.

Likewise, major findings on how changes in corrugation length affect the flow field are:

- At sufficiently low corrugation lengths (this corrugation length depends on the corrugation height), a re-circulation zone filling up most of the corrugated section is present.

- At a slightly higher corrugation length, the swirl velocity is increased while the re-circulation zone is decreased. The result is increased Nusselt number and friction factor.

- When increasing the corrugation length further, the re-circulation zone is completly eliminated while the swirl is increased to its maximum. This is the point resulting in the highest Nusselt number.

- As the corrugation length is further increased, the swirl starts to decrease as the tube approaches the non-corrugated tube.

By comparing the flow field to the Nusselt number and Darcy-Weisbach friction factor, the results show that the radically different flow field at high corrugations only increases the heat transfer slightly at a significant increase in pressure loss. In general, the tubes without stream-wise re-circulating flow seems to be optimal for transferring heat at constant pumping power when comparing to a non-corrugated tube.

Furthermore, tubes having a high swirling velocity combined with eliminated re-circulation zones are expected to be less prone to particulate deposition. Therefore, further numerical or experimental studies could be focused on investigating the optimal tube by a combination of Nusselt number, friction factor and tendency to deposit particulate matter.

Acknowledgement

References

[1] S. Ganeshan, M. R. Rao, Studies on thermohydraulics of single- and multi-start spirally corrugated tubes for water and time-independent power law fluids, International Journal of Heat and Mass Transfer 25 (1982) 1013–1022, DOI: http://dx.doi.org/10.1016/0017-9310(82)90076-X.

[2] V. D. Zimparov, N. L. Vulchanov, L. B. Delov, Heat transfer and friction characteristics of spirally corrugated tubes for power plant condensers — 1. Experimental investigation and performance evaluation, International Journal of Heat and Mass Transfer 34 (1991) 2187–2197, DOI: http://dx.doi.org/10.1016/0017-9310(91)90045-G.

[3] S. Rainieri, G. Pagliarini, Convective heat transfer to temperature dependent property fluids in the entry region of corrugated tubes, International Journal of Heat and Mass Transfer 45 (2002) 4525–4536, DOI: http://dx.doi.org/10.1016/S0017-9310(02)00156-4.

[4] R. Bhadouriya, A. Agrawal, S. Prabhu, Experimental and numerical study of fluid flow and heat transfer in a twisted square duct, International Journal of Heat and Mass Transfer 82 (2015) 143–158, DOI: http://dx.doi.org/10.1016/j.ijheatmasstransfer.2014.11.054.

[5] X. S. Tan, D. S. Zhu, G. Y. Zhou, L. Yang, 3D numerical simulation on the shell side heat transfer and pressure drop performances of twisted oval tube heat exchanger, International Journal of Heat and Mass Transfer 65 (2013) 244–253, DOI: http://dx.doi.org/10.1016/j.ijheatmasstransfer.2013.06.011.

[6] R. Zheng, N. Phan-Thien, R. Tanner, M. Bush, Numerical analysis of viscoelastic flow through a sinusoidally corrugated tube using a boundary element method, Journal of Rheology 34 (1990) 79, DOI: http://dx.doi.org/10.1122/1.550115.

[7] Ö. Ağra, H. Demir, Ş. Ö. Atayılmaz, F. Kantaş, A. S. Dalkılıç, Numerical investigation of heat transfer and pressure drop in enhanced tubes, International Communications in Heat and Mass Transfer 38 (2011) 1384–1391, DOI: http://dx.doi.org/10.1016/j.icheatmasstransfer.2011.07.013.

[8] H.-Z. Han, B.-X. Li, B.-Y. Yu, Y.-R. He, F.-C. Li, Numerical study of flow and heat transfer characteristics in outward convex corrugated tubes, International Journal of Heat and Mass Transfer 55 (2012) 7782–7802, DOI: http://dx.doi.org/10.1016/j.ijheatmasstransfer.2012.08.007.

[9] H. A. Mohammed, A. K. Abbas, J. M. Sheriff, Influence of geometrical parameters and forced convective heat transfer in transversely corrugated circular tubes, International Communications in Heat and Mass Transfer 44 (2013) 116–126, DOI: http://dx.doi.org/10.1016/j.icheatmasstransfer.2013.02.005.

[10] H. Han, B. Li, W. Shao, Effect of flow direction for flow and heat transfer characteristics in outward convex asymmetrical corrugated tubes, International Journal of Heat and Mass Transfer 92 (2016) 1236–1251, DOI: http://dx.doi.org/10.1016/j.ijheatmasstransfer.2014.11.076.

[11] P. G. Vicente, A. García, A. Viedma, Experimental investigation on heat transfer and frictional characteristics of spirally corrugated tubes in turbulent flow at different Prandtl numbers, International Journal of

Heat and Mass Transfer 47 (2004) 671–681, DOI: http://dx.doi.org/10.1016/j.ijheatmasstransfer.2003.08.005.

[12] Z. S. Kareem, M. N. M. Jaafar, T. M. Lazim, S. Abdullah, A. F. Abdulwahid, Passive heat transfer enhancement review in corrugation, Experimental Thermal and Fluid Science 68 (2015) 22–38, DOI: http://dx.doi.org/10.1016/j.expthermflusci.2015.04.012.

[13] A. E. Bergles, A. R. Blumenkrantz, J. Taborek, Performance evaluation criterion for enhanced heat transfer surfaces, in: Proceedings of the 5th International Heat Transfer Conference, vol. 2, The Japan Society of Mechanical Engineers, 234–238, 1974.

[14] R. L. Webb, Performance evaluation criteria for use of enhanced heat transfer surfaces in heat exchanger design, International Journal of Heat and Mass Transfer 24 (1981) 715–726, DOI: http://dx.doi.org/10.1016/0017-9310(81)90015-6.

[15] S. Pethkool, S. Eiamsa-ard, S. Kwankaomeng, P. Promvonge, Turbulent heat transfer enhancement in a heat exchanger using helically corrugated tube, International Communications in Heat and Mass Transfer 38 (2011) 340–347, DOI: http://dx.doi.org/10.1016/j.icheatmasstransfer.2010.11.014.

[16] V. Gnielinski, New equations for heat and mass transfer in turbulent pipe and channel flow, Int. Chem. Eng 16 (1976) 359–368, DOI: http://dx.doi.org/10.1007/BF02559682.

[17] G. Filonenko, Hydraulischer Widerstand von Rohrleitungen, Teploenergetika 1 (1960) 1098–1099.

[18] W. Hufschmidt, E. Burck, Der einfluss temperaturabhängiger stoffwerte auf den wärmeübergang bei turbulenter strömung von flüssigkeiten in rohren bei hohen wärmestromdichten und prandtlzahlen, Int. J. Heat Mass Transfer 11 (1968) 1041–1104, DOI: http://dx.doi.org/10.1016/0017-9310(68)90009-4.

[19] V. Jakovlev, Örtliche und mittlere Wärmeübetragung bei turbulenter Rohrströmung nichtsiedenden Wassers und hohen Wärmebelastungen, Kernenergie 3 (1960) 1098–1099.

[20] F. R. Menter, R. Langtry, S. Vølker, Transition Modelling for General Purpose CFD Codes, Flow Turbulence Combust 77 (2006) 277–303, DOI: http://dx.doi.org/10.1007/s10494-006-9047-1.

[21] F. R. Menter, Improved Two-Equation k-omega Turbulence Models for Aerodynamic Flows, Tech. Rep., National Aeronautics and Space Administration, 1992.

[22] S. V. Patankar, C. H. Liu, E. M. Sparrow, Fully Developed Flow and Heat Transfer in Ducts Having Streamwise-Periodic Variations of Cross-Sectional Area, Journal of Heat Transfer 99 (1977) 180–186, DOI: http://dx.doi.org/10.1115/1.3450666.

[23] P. J. Roache, Perspective: A Method for Uniform Reporting of Grid Refinement Studies, Journal of Fluids Engineering 116 (1994) 405–413, DOI: http://dx.doi.org/10.1115/1.2910291.

Nomenclature

A	Cross-sectional area
C_{p}	Pressure coefficient
D	Pipe diameter
e	Corrugation height
f	Darcy–Weisbach friction factor
h	Convective heat transfer coefficient
k	Thermal conductivity
L	Length of pipe section
p	Pressure
p	Corrugation length
Pr	Prandtl number
Re	Reynolds number
T	Temperature
u	Fluid velocity
y^{+}	Dimensionless wall distance

Greek letters

η	Thermal performance parameter
μ	Dynamic viscosity
ν	Kinematic viscosity
ρ	Density
τ	Wall shear stress
ϕ	Axial flow parameter
ψ	Swirling flow parameter

Subscripts

b	Bulk values
s	non-corrugated reference pipe
w	Wall values
z	Local coordinate along pipe length

Acronyms

CFD	Computational Fluid Dynamics
GCI	Grid Convergence Index
SST	Shear-Stress Transport
URANS	Unsteady Reynolds-averaged Navier-Stokes